LCLS-II Technical Note

Soft X-ray Self Seeding with one- and two-color gratings at LCLS-II

LCLS-II-TN-21-05

(Jun. 2021, R1.0)

Erik Hemsing and Alex Halavanau

(SLAC)

The soft x-ray self seeding system (SXRSS-II) at the LCLS-II (linac coherent light source) is studied for both monochromatic and two-color self seeding operations. We briefly review the relevant diffraction grating theory, including the associated linear matrix transport formalism for finite pulses, and then analyze the design and performances characteristics of a two-color grating.

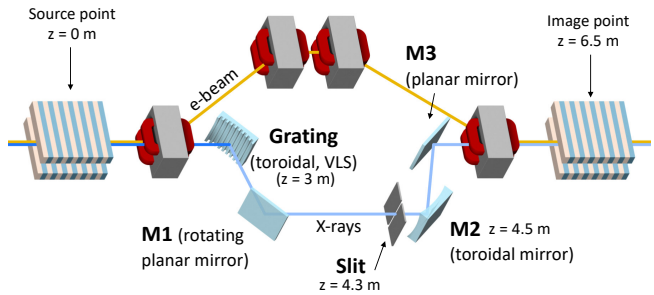

FIG. 1: LCLS-II soft x-ray self-seeding system layout (not to scale). The electron beam is propagated through the chicane magnets while the photon beam is sent onto the grating and through the imaging system. The first diffraction order ($m = 1$) is apertured at the slit, propagated and refocused onto the electron beam downstream [2].

I. INTRODUCTION

Soft X-ray self-seeding (SXRSS) has been successfully built [1–3] and commissioned at the LCLS [4] free electron laser (FEL). It is currently planned for re-commissioning with the new LCLS-II variable gap undulators. In the present configuration (Fig. 1), the SXRSS system consists of a grazing incidence toroidal diffraction grating with varied line spacing (VLS), a rotating mirror (M1), a collimation slit, a focusing spherical mirror ($M2$), and a plane mirror (M3). This setup enhances the SXR beam coherence properties and is a core x-ray science capability for high resolution studies. It is also a topic of active FEL study [5–8].

Here we examine a few aspects of SXRSS as they apply to LCLS-II. First, in Sec. II, we review the standard grating theory, which is used to numerically model x-ray transport through the SXRSS system. While the baseline optical design is essentially unchanged from the LCLS design, the new variable gap LCLS-II SXR undulators provide a new flexibility in the range of electron beam energies can produce the same SXR photon energy. As such, the effective SASE source point and size in the undulators upstream of the SXRSS (positioned at the U10 position) can vary, which impacts the downstream spectral imaging for seeding in the downstream undulator (U11). We outline two basic approaches to modeling the system; the light path function, which yields the different expansion orders of the Fresnel integral transport equations, and the matrix formalism of Kostenbauder [9] which provides a straightforward way to model Gaussian pulses through the linear optics. The matrix formalism is an approximation of the Fresnel approach (which applies to all orders and for arbitrary beam distributions), but is still useful.

Second, in Sec. VI, we examine a two-color grating design that interleaves rulings of different density across the SXRSS grating. This grating has the same VLS parameters and toroidal substrate as the existing single color grating except it is ruled to send two colors within the SASE bandwidth into the same forward angle. This produces two-color seeded FEL pulses with fixed 0.1% relative color separations and a temporal intensity modulation. Dual- and multi-color gratings are well-known in laser optics (e.g., [10, 11]), but have not yet been applied for SXR self-seeding schemes in XFELs. At hard x-rays, multicolor seeding has been achieved by exploiting overlapping crystal reflections [12]. At soft x-rays, multi-color self-seeding combined with a recently proposed enhanced self-seeding approach [13] could lead to a stable multi-color SXR source, opening new possibilities in time-dependent polarization control [14] or new science applications (e.g., [15–17]).

II. TOROIDAL VLS GRATING THEORY

An illustration of the coordinate system for the grating is shown in Fig. 2. The incident field is emitted from the object point A (the source position in the upstream undulator), diffracted from point P at the location $\mathbf{r}_0 = (x_0, y_0, z_0)$ on the grating surface, and focused to the point B (slit). The typical approach for analyzing the spectral and focusing properties of the grating is through the light path function, which boils down to minimizing the accumulated phase differences over the different paths. The light path function is [18]

$$F = \overline{AP} + \overline{PB} + nm\lambda \tag{1}$$

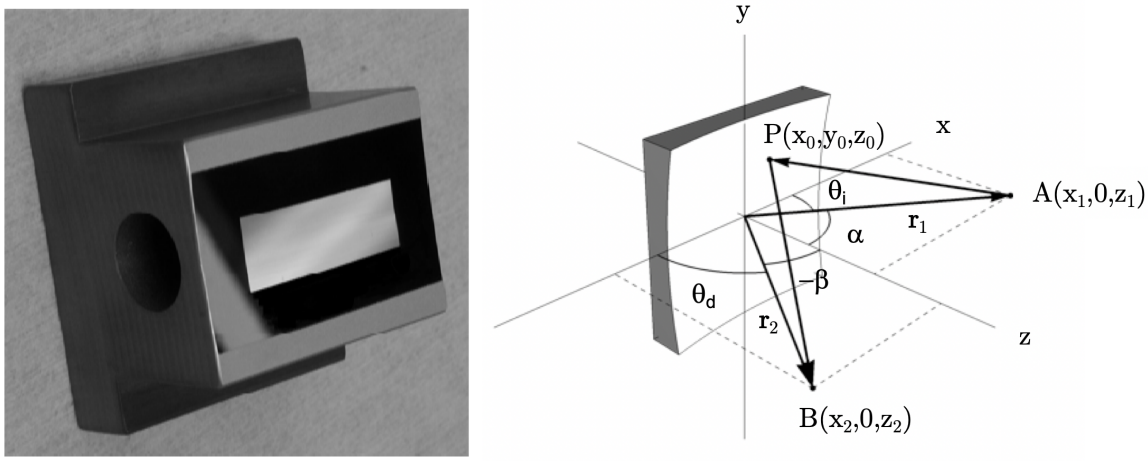

FIG. 2: Left: Picture of the SXRSS grating from [1]. Right: Schematic diagram of the toroidal grating coordinate system with the source point at A, and the image point at B.

where n is the groove number at the point P, m is the diffraction order, and λ is the wavelength. The image is obtained when the conditions

$$\frac{\partial F}{\partial x_0} = 0, \qquad \frac{\partial F}{\partial y_0} = 0 \tag{2}$$

are satisfied. We define the incident angle $\theta_i = \pi/2 - \alpha$ and diffraction angle $\theta_d = \pi/2 + \beta$ with respect to the grating substrate surface such that

$$\begin{aligned} x_1 &= r_1 \sin\alpha = r_1 \cos\theta_i \\ x_2 &= r_2 \sin\beta = -r_2 \cos\theta_d \\ z_1 &= r_1 \cos\alpha = r_1 \sin\theta_i \\ z_2 &= r_2 \cos\beta = r_2 \sin\theta_d. \end{aligned} \tag{3}$$

The path distances are given by

$$\begin{aligned} \overline{AP}^2 &= |\mathbf{r}_0 - \mathbf{r}_1|^2 = (x_0 - x_1)^2 + y_0^2 + (z_0 - z_1)^2 = r_1^2 + x_0^2 + y_0^2 + z_0^2 - 2r_1 x_0 \cos\theta_i - 2r_1 z_0 \sin\theta_i \\ \overline{PB}^2 &= |\mathbf{r}_2 - \mathbf{r}_0|^2 = (x_2 - x_0)^2 + y_0^2 + (z_2 - z_0)^2 = r_2^2 + x_0^2 + y_0^2 + z_0^2 + 2r_2 x_0 \cos\theta_d - 2r_2 z_0 \sin\theta_d \end{aligned} \tag{4}$$

The ruled grating surface, measured by the largest extent of $|\mathbf{r}_0|$ (which is 20×4 mm for the SXRSS design in the tangential and sagittal planes respectively) is much smaller than the distances to the source r_1 and image r_2. Thus we can expand the light paths to different orders in the components of $\mathbf{r}_0$,

$$\begin{aligned} \overline{AP} &= r_1 - x_0 \cos\theta_i + \frac{x_0^2}{2}\left(\frac{\sin^2\theta_i}{r_1} - \frac{\sin\theta_i}{R_1}\right) + \frac{y_0^2}{2}\left(\frac{1}{r_1} - \frac{\sin\theta_i}{\rho}\right) + \dots \\ \overline{PB} &= r_2 + x_0 \cos\theta_d + \frac{x_0^2}{2}\left(\frac{\sin^2\theta_d}{r_2} - \frac{\sin\theta_d}{R_1}\right) + \frac{y_0^2}{2}\left(\frac{1}{r_2} - \frac{\sin\theta_d}{\rho}\right) + \dots \end{aligned} \tag{5}$$

We have used the equation for a torus as depicted in FIG. 2, sitting in the $x - z$ plane, with an outer edge just touching the $x - y$ plane,

$$\left(\sqrt{x_0^2 + (z_0 - R_1)^2} - (R_1 - \rho)\right)^2 + y_0^2 = \rho^2. \tag{6}$$

where ρ is the radius of curvature in the poloidal direction (i.e., the sagittal/vertical focusing), and R_1 is the radius of curvature in the toroidal direction (tangential/horizontal focusing). Solving for z_0 and about the origin $(x_0, y_0) = (0, 0)$, we can write z_0 to lowest order in terms of x_0 and y_0,

$$z_0 \approx \frac{x_0^2}{2R_1} + \frac{y_0^2}{2\rho}. \tag{7}$$

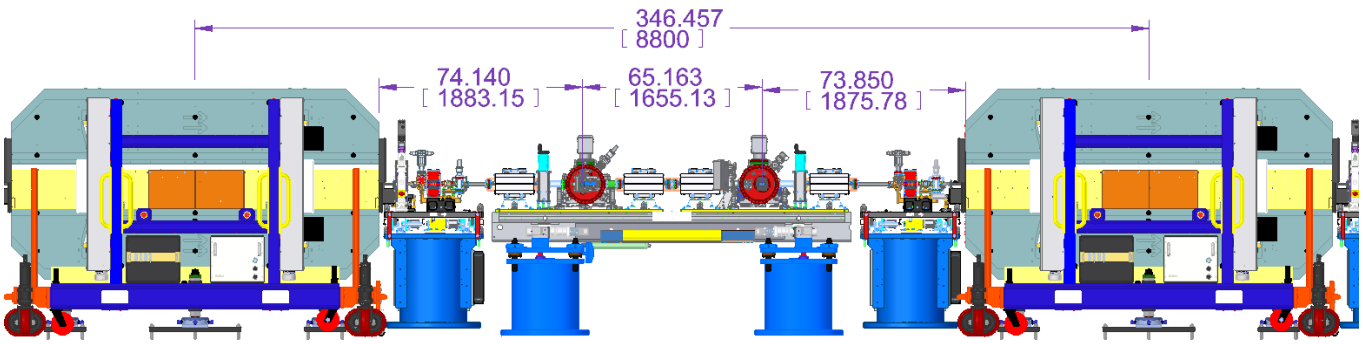

FIG. 3: SXRSS system in the U10 position between undulators. Beam travels left to right. Measurements are in inches [mm]. The distance from the exit of U9 to the grating is 1883 mm, and from $M3$ to the entrance of U11 is 1876 mm.

The shape is parabolic near the origin.

A grating with varied line spacing (VLS) has a groove density of the form

$$\frac{dn}{dx_0} = N(x_0) = N_0 + N_1 x_0 + N_2 x_0^2. \tag{8}$$

where N_1 introduces diffraction focusing and N_2 corrects for aberration.

Combining Eqs. (5) and (8) the light path function can then be written to different orders

$$F = r_1 + r_2 + C_{1,0}x_0 + C_{2,0}x_0^2 + C_{0,2}y_0^2 + C_{1,2}x_0y_0^2 + C_{3,0}x_0^3 + \dots \tag{9}$$

with coefficients

$$\begin{aligned}
C_{1,0} &= m\lambda N_0 - \cos\theta_i + \cos\theta_d \\
C_{2,0} &= \frac{m\lambda N_1}{2} + \frac{\sin\theta_i}{2}\left(\frac{\sin\theta_i}{r_1} - \frac{1}{R_1}\right) + \frac{\sin\theta_d}{2}\left(\frac{\sin\theta_d}{r_2} - \frac{1}{R_1}\right) \\
C_{0,2} &= \frac{1}{2}\left(\frac{1}{r_1} - \frac{\sin\theta_i}{\rho} + \frac{1}{r_2} - \frac{\sin\theta_d}{\rho}\right) \\
C_{1,2} &= \frac{\cos\theta_i}{2r_1}\left(\frac{1}{r_1} - \frac{\sin\theta_i}{\rho}\right) - \frac{\cos\theta_d}{2r_2}\left(\frac{1}{r_2} - \frac{\sin\theta_d}{\rho}\right) \\
C_{3,0} &= \frac{m\lambda N_2}{3} + \frac{\sin\theta_i\cos\theta_i}{2r_1}\left(\frac{\sin\theta_i}{r_1} - \frac{1}{R_1}\right) - \frac{\sin\theta_d\cos\theta_d}{2r_2}\left(\frac{\sin\theta_d}{r_2} - \frac{1}{R_1}\right).
\end{aligned} \tag{10}$$

The principal ray is given according to where each coefficient vanishes.

A. Tangential Plane

The first term $C_{1,0} = 0$ yields the grating equation for the principle ray wavelength λ_0,

$$m\lambda_0 N_0 = \cos\theta_i - \cos\theta_d. \tag{11}$$

Moving forward we assume that $m > 0$. For grazing incidence and diffraction angles $\theta_i, \theta_d \ll 1$, then $\theta_d^2 \approx \theta_i^2 + 2m\lambda_0 N_0$ and the diffraction angle is larger than the incidence angle. Further, in the case of the SXRSS grating where $\theta_i^2 \ll 2m\lambda_0 N_0$ the diffraction angle is weakly dependent on the incident angle and scales like $\sqrt{\lambda_0}$,

$$\theta_d^2 \approx 2m\lambda_0 N_0. \tag{12}$$

This approximation will become useful for estimating the optimal VLS grating terms.

TABLE I: SXRSS parameters for LCLS-II. Distances given are for the light path. Values for N_1 and N_2 in parentheses are from the estimates presented in Eqs. (18) and (19). Note that the opposite sign of N_1 is due simply to our choice of coordinate system, and that the density increases along the direction of propagation.

Parameter	**Variable**	**Value**	**Unit**
X-ray photon energy	$\hbar\omega_0$	300–1200	eV
Wavelengths	λ	4–1	nm
Magnification parameter	μ	5.4–2.8	–
Source position	r_1	1.9–4.3 (+4.4 m w/U9 out)	m
U9 exit to grating	–	1.883	m
Grating to slit	r_2	1.35	m
Slit to $M2$	r_s	0.18	m
Grating to $M2$	r_{m2}	1.528	m
$M2$ to image point inside U11	r_3	3	m
$M3$ to U11 entrance	–	1.876	m
Grating incidence angle	θ_i	18.2 (1.04)	mrad (deg)
Grating diffraction angle	θ_d	100–50 (5.73–2.86)	mrad (deg)
Grating tang. rad. of curv	R_1	185	m
Grating tang. focal len.	f_{tan}	0.25–0.46	m
Grating sag. rad. of curv	ρ	0.18	m
Grating sag. focal len.	f_{sag}	1.55–2.6	m
Groove density	N_0	1123	1/mm
Linear VLS	N_1	1.6 (-1.5)	1/mm^2
Quadratic VLS	N_2	0.002 (0.0018)	1/mm^3
$M2$ rad. of curv	ρ_2	23.2	m
$M2$ Incidence angle	ϕ	15 (0.086)	mrad (deg)
$M2$ tang. focus	f_{L_H}	0.174	m
$M2$ sag. focus	f_{L_V}	$\geq$700	m

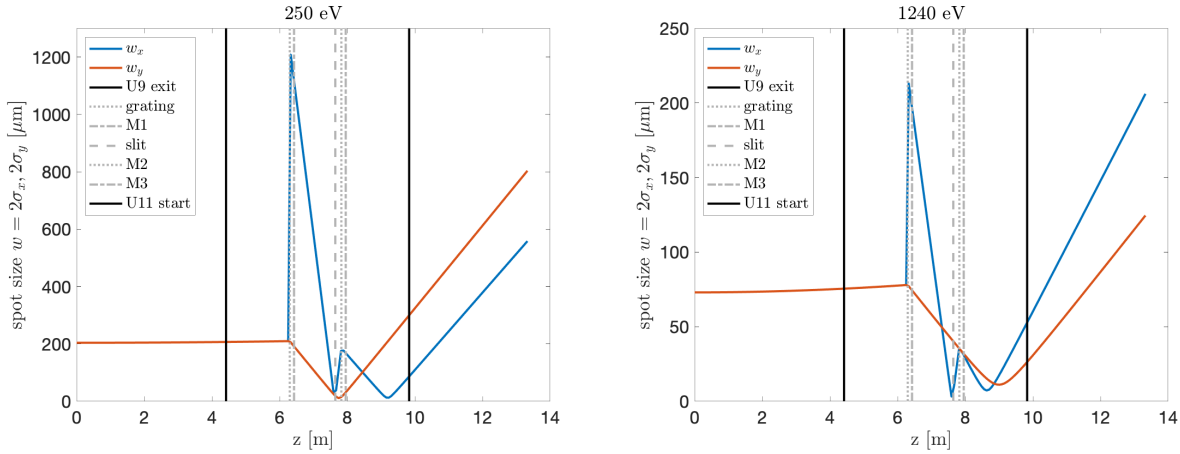

FIG. 4: Monochromatic X-ray pulse spot size evolution from source point through SXRSS system for 250 eV (left) and 1200 eV (right).

Setting $C_{2,0} = 0$ gives the tangential image location at the slit for the principal ray [1],

$$r_2 = \frac{r_1 \sin^2\theta_d}{\frac{r_1}{R_1}(\sin\theta_d + \sin\theta_i) - \sin^2\theta_i - m\lambda_0 r_1 N_1}. \tag{13}$$

Inverting this expression we can identify both the tangential focal length f_{tan}, and the effective rescaling of the source

point

$$\frac{1}{r_2} = \frac{1}{\mu f_{tan}} - \frac{1}{\mu^2 r_1} \tag{14}$$

where

$$\mu = \frac{\sin\theta_d}{\sin\theta_i} > 1 \tag{15}$$

is the tangential beam expansion parameter due to the different incidence and diffraction angles. The tangential focal length is explicitly,

$$f_{tan} = \frac{\sin\theta_i \sin\theta_d}{\frac{1}{R_1}(\sin\theta_i + \sin\theta_d) - m\lambda_0 N_1} \tag{16}$$

in agreement with Siegman in [19]. Note that in the Fourier propagation approach (Sec. V) the effective tangential focal length is rescaled to μf_{tan}, as given in [3].

The linear density variation N_1 is used to minimize the λ-dependent variation in the image position, which can be significant and impacts the seed bandwidth. By inspection of Eq. (10), a straightforward approach (which also assists in minimizing higher order aberrations) is to set the radius of tangential curvature close to

$$R_1 \approx \frac{r_1}{\sin\theta_i}. \tag{17}$$

Obviously this is approximate because the source distance is not fixed across the tuning range. As an estimate, however, we then set

$$N_1 = -\frac{\sin\theta_d}{m\lambda_0}\left(\frac{\sin\theta_d}{r_2} - \frac{\sin\theta_i}{r_1}\right) \approx -\frac{2N_0}{r_2} + \sqrt{\frac{2N_0}{m\lambda_0}}\frac{\theta_i}{r_1}. \tag{18}$$

We have used (12) in the last step. For the SXRSS grating the last term is small, so the dependence on the wavelength is weak. Using the parameters in Table II for $r_1 = 3.9$ m we obtain $R_1 = 215$ m and $N_1 = -1.5$ mm^{-2}, close to the values of the existing SXRSS grating. Note that this value of N_1 is the opposite sign of that defined in the SXRSS PRD and associated literature due to the way we have defined the grating coordinate system with the source point A in the $x_0 > 0$ region, and the image point B in the $x_0 < 0$ region. Both are consistent as in both cases, the groove density increases in the direction of beam propagation (see FIG. 8).

The spherical aberration in the tangential plane vanishes if $C_{3,0} = 0$. Again using (17), we can then force $C_{3,0} = 0$ (at least for the principal ray) with

$$N_2 = \frac{3\sin\theta_d\cos\theta_d}{2m\lambda_0 r_2}\left(\frac{\sin\theta_d}{r_2} - \frac{1}{R_1}\right) = -3N_1\frac{\cos\theta_d}{2r_2} \approx 3\frac{N_0}{r_2^2} \tag{19}$$

With the parameters in Table II we obtain $N_2 = 0.0018$ mm^{-3}. This is slightly less than the 0.002 value specified for the SXRSS, but the system is fairly insensitive to this parameter.

B. Sagittal Plane

The image position r_2 in the vertical plane is given by $C_{0,2} = 0$. This yields the typical expression for the sagittal focal length f_{sag} of a curved grating surface [19],

$$\frac{1}{r_1} + \frac{1}{r_2} = \frac{\sin\theta_i + \sin\theta_d}{\rho} \equiv \frac{1}{f_{sag}}. \tag{20}$$

The basic formalism can be straightforwardly extended to include the non-dispersive focusing optics such as $M2$ downstream.

C. Summary

The light path formalism provides a straightforward way to extract and optimize the optical transport via point-to-point imaging. For beams with finite size and bandwidth one can use increasingly more sophisticated descriptions, starting with the ABCD matrix formalism and its extension to finite pulse durations, and ending with a full Fresnel propagation integral that can also include higher order aberrations and arbitrary paraxial wave input fields.

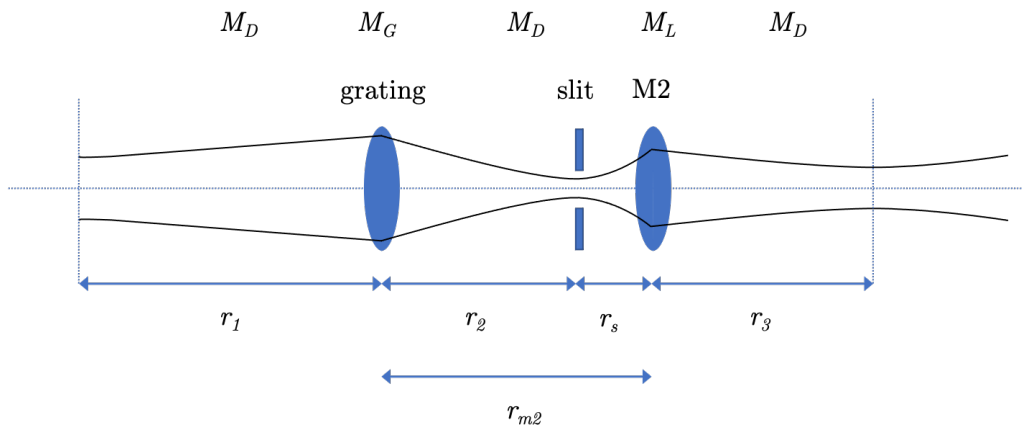

FIG. 5: SXRSS imaging layout and associated transport matrices (not to scale).

III. ABCD FORMALISM

The ABCD matrix formalism is a simple way to investigate the linear aspects of the SXRSS transport for a monochromatic beam with finite spatial extent without needing the full Fourier propagation approach. It yields approximate values for the spot sizes of the image point downstream of the SXRSS system, including the corrections for finite Rayleigh lengths $z_R = \pi w_0^2/\lambda$. An extension for non-monochromatic beams is summarized in Sec. IV. We note that here we only consider idealized single mode beams with M^2=1, whereas the actual incoming SASE pulses may be multi-moded with $M^2 \approx 3-4$. This generalization can also be explored with the ABCD formalism [20], but we avoid it here in part for simplicity, but also because the beam is strongly dispersion-dominated after the grating, which is what determines most of the salient features of the SXRSS system (such as resolving power).

The transverse envelope evolution from the x-ray source point to the seed image point is shown in Fig. 5. The linear transport can be modeled as a transformation on a Gaussian beam $\exp\left(-ik\frac{x^2}{2q}\right)$ characterized by the complex parameter

$$\frac{1}{q} = \frac{1}{R_c} - i\frac{\lambda}{\pi w^2} \tag{21}$$

where R_c is the source x-ray pulse radius of curvature and w is the spot size. Assuming a Gaussian guided mode in the high gain regime, these can be approximated from 3D FEL theory as [21]

$$w = 2\sigma_x \left(\frac{L_{3D}}{2k\sigma_x^2}\right)^{1/4}, \qquad R_c = -1.86 L_{3D}\left(\frac{L_{3D}}{2k\sigma_x^2}\right)^{-1/2} \tag{22}$$

where $\sigma_x = \sqrt{\epsilon_n \beta/\gamma}$ is the rms transverse electron beam size, $\lambda = 2\pi/k$ is the wavelength, and L_{3D} is the 3D power gain length. Given a total transport matrix

$$M = \begin{pmatrix} A & B \\ C & D \end{pmatrix}, \tag{23}$$

the characteristics of the monochromatic Gaussian output beam are given by

$$q_f = \frac{Aq_i + B}{Cq_i + D} \tag{24}$$

The final beam's radius of curvature and spot size can be obtained straightforwardly from $R_{cf} = 1/\mathrm{Re}\,(1/q_f)$ and $w_f^2 = -\lambda/\pi \mathrm{Im}\,(1/q_f)$ with the known elements of M and the initial beam complex-valued q_i at the end of the upstream undulator. Alternatively, and for simplicity of the analysis, one can calculate the position z_s and waist size w_0 of the effective x-ray beam source point inside the undulator where $q_i = iz_R$ where $z_R = \pi w_0^2/\lambda$ is the Rayleigh length with

$$w_0^2 = \frac{4R_c^2 w^2}{4R_c^2 + k^2 w^4}, \qquad z_s = w_0^2 \frac{k^2 w^2}{4R_c}. \tag{25}$$

TABLE II: Electron and X-ray beam parameters for LCLS-II. The SXRSS system is positioned in the U10 undulator slot. Parameters in parentheses are for a SASE beam that has not reached full FEL gain-guiding (and may contain multiple transverse modes), compared to an ideal guided beam.

Parameter	**Variable**	**Value**	**Unit**
e-beam Energy	γmc^2	4	GeV
e-beam Current	-	1.0	kA
e-beam ave. beta func	β	18	m
e-beam norm emit.	ϵ_n	0.35	mm mrad
e-beam ave. size	σ_x	28	μm
undulator segment length	-	3.4+1.0 drift	m
effective gain length	L_{3D}	1.8–2.7	m
effective FEL parameter	ρ_{3D}	1.0–0.66	10^{-3}
x-ray photon energy	$\hbar\omega_0$	300–1200	eV
x-ray source waist size	w_0	47–37 (197–67)	μm
x-ray source waist pos. inside und.	z_s	-0.9– -2.4 (-3.5)	m
x-ray spot size at grating	–	100–50 (204–73)	μm

The distance from the end of U9 to the grating surface at LCLS-II is 1.883 m, so the distance from the source point to the grating in this approach is $r_1 = 1.883 - z_s = 1.9$ to 4.3 m (z_s is typically negative because $R_c < 0$).

The matrix for a drift length r_1 is given by

$$M_D(r_1) = \begin{pmatrix} 1 & r_1 \\ 0 & 1 \end{pmatrix} \tag{26}$$

The x-ray beam then encounters the grating, which treats the horizontal and vertical planes differently. The matrices are,

$$M_{G_H} = \begin{pmatrix} \mu & 0 \\ -1/f_{tan} & 1/\mu \end{pmatrix}, \qquad M_{G_V} = \begin{pmatrix} 1 & 0 \\ -1/f_{sag} & 1 \end{pmatrix}. \tag{27}$$

where $\mu = \sin\theta_d/\sin\theta_i > 1$ is the tangential beamwidth expansion parameter in Eq. (15). The beam then drifts a length $r_{m2} = r_2 + r_s = 1.528$ m through the slit to the spherical focusing mirror $M2$. The $M2$ focusing is modeled by the focusing matrices

$$M_{L_{H,V}} = \begin{pmatrix} 1 & 0 \\ -1/f_{L_{H,V}} & 1 \end{pmatrix} \tag{28}$$

where $f_{L_H} = (\rho_2 \sin\phi)/2$ and $f_{L_V} = \rho_2/(2\sin\phi)$ with radius of curvature ρ_2 at an incidence angle ϕ (See Table II). In the present design, the vertical focusing effect from $M2$ is negligible so we can take the $f_{L_V} \to \infty$ limit. $M2$ is followed by a drift r_3 into the seed undulator. The associated waist position varies somewhat with wavelength due to the dependence of f_{tan} and f_{sag} in (16) and (20) on the diffracted angle. The total transport matrices are

$$\begin{aligned} M_H &= M_D(r_3) M_{L_H} M_D(r_{m2}) M_{G_H} M_D(r_1) \\ M_V &= M_D(r_3) M_{L_V} M_D(r_{m2}) M_{G_V} M_D(r_1) \end{aligned} \tag{29}$$

It can be shown that for a source beam at a waist ($q_i = iz_R$), the location of the final waist position is given by the solution to $ACz_R^2 + BD = 0$ of the total transport matrix. Assuming that the Rayleigh length of the initial beam is large compared to the individual drift and focal lengths in the system, the waist position in the horizontal plane is given approximately by

$$r_{3,H} \approx \frac{f_{L_H}(r_{m2} - \mu f_{tan})}{(r_{m2} - \mu f_{tan}) - f_{L_H}} \tag{30}$$

where, by design, $r_{m2} - \mu f_{tan} \approx r_s$ is approximately the distance from the slit to $M2$. Thus the slit is being imaged horizontally by $M2$ toward the U11 undulator entrance. The waist position in the vertical dimension has the exact

form

$$r_{3,V} = f_{sag} - r_{m2} + \frac{f_{sag}^2(r_1 - f_{sag})}{(r_1 - f_{sag})^2 + z_R^2} \tag{31}$$

where in the present design with weak vertical $M2$ focusing the slit is not being imaged vertically. From these expressions one can define the horizontal magnification $\mu_H = -r_{3,H}/(r_{m2} - \mu f_{tan})$ of the slit plane,

$$\mu_H = \frac{f_{L_H}}{f_{L_H} + \mu f_{tan} - r_{m2}}. \tag{32}$$

The vertical magnification is one since the slit is not imaged vertically.

Assuming an initially round beam with a Rayleigh length long compared to the drift lengths, the spot sizes at the waists downstream of the SXRSS system for a monochromatic input beam are given by

$$w_x^2 = w_0^2 \frac{A^2 z_R^2 + B^2}{z_R^2} \approx \left(\frac{w_0 f_{tan} \mu_H}{z_R}\right)^2, \quad w_y^2 \approx \left(\frac{w_0 f_{sag}}{z_R}\right)^2. \tag{33}$$

The spot size evolution through the SXRSS system for a monochromatic beam is shown in Fig (4), where one can identify the waist sizes and locations just upstream of the U11 undulator entrance.

IV. ABCD EXTENSION FOR FINITE PULSE DURATIONS

The linear ABCD transport formalism can be extended to pulses of finite temporal duration to assess the spectral properties of the transport, including the resolving power of the SXRSS system. Kostenbauder [9] describes an elegant generalized description for Gaussian pulses that starts with the expanded transformation matrix M,

$$\begin{pmatrix} x \\ \theta \\ t \\ f_0 \end{pmatrix}_{out} = \begin{pmatrix} A & B & 0 & E \\ C & D & 0 & F \\ G & H & 1 & I \\ 0 & 0 & 0 & 1 \end{pmatrix} \begin{pmatrix} x \\ \theta \\ t \\ f_0 \end{pmatrix}_{in} = M \begin{pmatrix} x \\ \theta \\ t \\ f_0 \end{pmatrix}_{in}. \tag{34}$$

The spatial variables (x, θ) here refer to the transverse coordinates of the optical beam in the plane orthogonal to the direction of propagation, as distinct from the coordinate system defined by the grating in Fig (2). The matrix element $E = \partial x_{out}/\partial f_{in}$ is the spatial chirp, $F = \partial \theta_{out}/\partial f_{in}$ is the angular dispersion, $G = \partial t_{out}/\partial x_{in}$ is the pulse front tilt, $H = \partial t_{out}/\partial \theta_{in}$ is the time/angle correlation, and $I = \partial t_{out}/\partial f_{in}$ is the group delay dispersion, GDD. A general extension to the vertical dimension is given in [22].

Following Kostenbauer, the elements of M can be used to calculate the transformation of a beam with Gaussian spatial and temporal distributions through the linear system. Consider a general bi-Gaussian pulse of the form

$$E(x,t) \propto \exp\left[-i\frac{k_0}{2}\begin{pmatrix} x \\ -t \end{pmatrix}^T Q^{-1} \begin{pmatrix} x \\ t \end{pmatrix}\right] = \exp\left[i\frac{k_0}{2\,\mathrm{Det}(Q)}\left(Q_{xx}t^2 + 2Q_{xt}tx - Q_{tt}x^2\right)\right] \tag{35}$$

where $Q_{21} = Q_{tx} = -Q_{xt}$. This is an extension of the previous Gaussian beam description that uses the complex parameter q. Here, however Q is a matrix that includes the temporal features as well as the spatial-temporal cross terms Q_{xt} when the dispersion is non-zero. For example, consider an uncorrelated input beam at a waist $E_0(x,t) = \exp\left[-x^2/w_0^2 - t^2/4\sigma_t^2\right]$. From (35) the input matrix Q_i is simply

$$Q_i = \begin{pmatrix} iz_R & 0 \\ 0 & -2ik_0\sigma_t^2 \end{pmatrix}. \tag{36}$$

Whatever the form of the input Q_i, the output matrix is related to the input matrix via the transport elements of M,

$$Q_f = \frac{\left[\begin{pmatrix} A & 0 \\ G & 1 \end{pmatrix} Q_i + \begin{pmatrix} B & E/\lambda_0 \\ H & I/\lambda_0 \end{pmatrix}\right]}{\left[\begin{pmatrix} C & 0 \\ 0 & 0 \end{pmatrix} Q_i + \begin{pmatrix} D & F/\lambda_0 \\ 0 & 1 \end{pmatrix}\right]}. \tag{37}$$

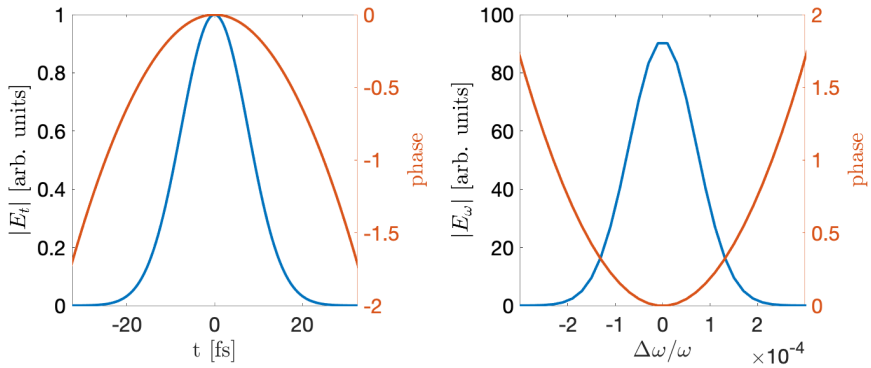

FIG. 6: Temporal (left) and spectral (right) pulse amplitudes on-axis at the U11 entrance of a $\sigma_\omega/\omega_0 = 0.1\%$ rms bandwidth Gaussian input pulse at 1240 eV, assuming an ideal, guided input from U9.

Division is multiplication by the inverse. Note the similarity with Eq. (24). Thus for a given Q_i and transport matrix M, one can calculate the output field in (35) with (37). The moments of the intensity distribution can also be calculated. For instance, from Eq. (35) the rms pulse duration and transverse size are given by

$$\langle t^2 \rangle = -\frac{\mathrm{Im}[\mathrm{Det}(Q)Q^*_{tt}]}{2k_0\,\mathrm{Det}(\mathrm{Im}[Q])}, \qquad \langle x^2 \rangle = \frac{\mathrm{Im}[\mathrm{Det}(Q)Q^*_{xx}]}{2k_0\,\mathrm{Det}(\mathrm{Im}[Q])}. \tag{38}$$

With the field in (35) we can obtain several properties about the beam that are completely general for any characteristic matrix Q. In the spectral domain $\tilde{E}(x,\Delta\omega) = \int E(x,t)e^{-i\Delta\omega t}dt$ the field near the principle frequency is

$$\tilde{E}(x,\Delta\omega) \propto \exp\left[-\frac{i}{2k_0 Q_{xx}}\left(\mathrm{Det}(Q)\Delta\omega^2 - 2k_0 Q_{xt}x\Delta\omega + k_0^2 x^2\right)\right]. \tag{39}$$

At the $x = 0$ centerline (e.g., a slit or the narrow electron beam in the SXRSS) the relative rms spectral bandwidth is

$$\frac{\sigma^2_{k,x=0}}{k_0^2} = \frac{1}{2k_0 c^2\,\mathrm{Im}\left[-\frac{\mathrm{Det}(Q)}{Q_{xx}}\right]}. \tag{40}$$

This will be useful for calculating the approximate resolving power of the SXRSS system. If $\mathrm{Re}\left[\frac{\mathrm{Det}(Q)}{Q_{xx}}\right] \neq 0$, then the pulse has quadratic phase components in both the frequency and time domains, and they are of opposite sign. An example from simulations of the SXRSS system at 1240 eV is shown in Fig. 6. This means that the on-axis seed pulse is frequency-chirped, with the instantaneous frequency given by the derivative of the temporal phase,

$$\omega(t) = \omega_0 + \mathrm{Re}\left[\frac{Q_{xx}}{\mathrm{Det}(Q)}\right]k_0 t = \omega_0\left(1 + \chi t\right). \tag{41}$$

where $\chi = \mathrm{Re}\left[\frac{Q_{xx}}{c\mathrm{Det}(Q)}\right]$ is the chirp. As such, the seed pulse duration is longer than the transform-limited duration σ_t by the factor $1/\sqrt{k_0\mathrm{Im}[Q_{xx}/\mathrm{Det}(Q)]}$.

A. SXRSS System

We now return to the specific case of the SXRSS system. The drift and grating matrices are, respectively [9, 19]

$$M_D(z) = \begin{pmatrix} 1 & z & 0 & 0 \\ 0 & 1 & 0 & 0 \\ 0 & 0 & 1 & 0 \\ 0 & 0 & 0 & 1 \end{pmatrix}, \qquad M_{G_H} = \begin{pmatrix} \mu & 0 & 0 & 0 \\ -\frac{1}{f_{tan}} & \frac{1}{\mu} & 0 & -\frac{\lambda_0^2 N_0}{c\mu\sin(\theta_i)} \\ -\frac{\lambda_0 N_0}{c\sin(\theta_i)} & 0 & 1 & 0 \\ 0 & 0 & 0 & 1 \end{pmatrix}. \tag{42}$$

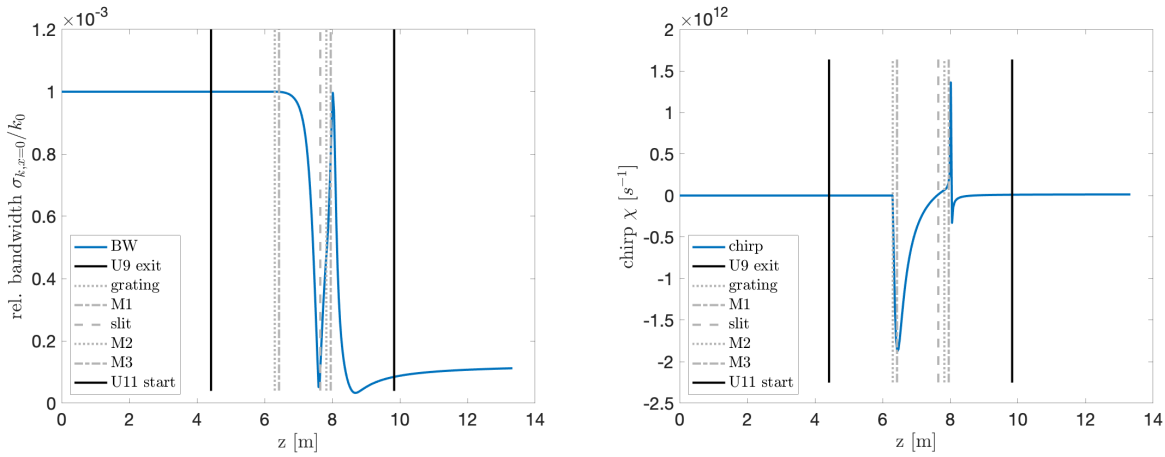

FIG. 7: On-axis relative bandwidth (left) and frequency chirp (right) for $\sigma_\omega/\omega_0 = 0.1\%$ rms bandwidth Gaussian input pulse at 1240 eV. Both vary considerably within the SXRSS system and then settle to stable values downstream in U11.

The signs of the matrix elements are chosen to be consistent with the present notation. Optical elements with pure focusing and no dispersion (e.g., $M2$ mirror or sagittal grating plane) use the same form of M_{G_H} with $N_0 = 0$ and $\mu = 1$. The total linear transport matrix in (29) from the source to the image point inside the undulator gives a Q_f in the horizontal plane of

$$Q_{f,H} = \frac{1}{\nu}\begin{pmatrix} (f_{tan} - q_1\mu)f_{L_H}^2 + (r_3 - f_{L_H})\nu & \frac{f_{tan} f_{L_H} N_0 q_1 \lambda_0 \mu}{c \sin\theta_i} \\ -\frac{f_{tan} f_{L_H} N_0 q_1 \lambda_0 \mu}{c \sin\theta_i} & -\frac{2 f_{tan} N_0^2 (f_{L_H} - r_{m2}) q_1 \lambda_0^2}{2c^2 \sin^2\theta_i} - \frac{ik\nu}{2c^2\sigma_k^2} \end{pmatrix} \tag{43}$$

where $q_1 = r_1 + iz_R$ and $\nu = f_{tan}\left(f_{L_H} - q_1\mu^2 - r_{m2}\right) + \mu(r_{m2} - f_{L_H})q_1$. In the vertical plane things are simpler,

$$Q_{f,V} = \begin{pmatrix} r_3 + r_{m2} + \frac{f_{sag} q_1}{f_{sag} - q_1} & 0 \\ 0 & -\frac{ik}{2c^2\sigma_k^2} \end{pmatrix}. \tag{44}$$

Using Eq. (40) the bandwidth of the on-axis seed field can be calculated. One may be tempted to calculate the bandwidth through at the slit which, assuming that the tangential focusing is $f = \frac{\mu r_1 r_2}{\mu^2 r_1 + r_2}$ from Eqs. (14) and (16), yields

$$\frac{\sigma_{k,slit}^2}{k_0^2} = \frac{\sigma_k^2/k_0^2}{1 + \left(\frac{4\pi N_0 \sigma_k r_1}{k_0^2 w_0 \sin\theta_i}\right)^2} \approx \left(\frac{k_0 w_0 \sin\theta_i}{4\pi N_0 r_1}\right)^2.$$

Here $\sigma_k = 1/2\sigma_t c$ is the bandwidth of the initial pulse which is assumed large enough that the beam is dispersion-dominated at the slit. However, it is the subsequent imaging of the slit by the $M2$ mirror into the downstream undulator that sets the ultimate seed bandwidth. This calculation uses $Q_{f,H}$ above and is a bit more involved, giving

$$\frac{\sigma_{k,x=0}^2}{k_0^2} \approx \left(\frac{\sin\theta_i}{2\pi N_0 w_0}\right)^2 \left[1 + \Delta f_H \frac{2r_1}{f_{tan}} + \frac{(\Delta f_H)^2}{f_{tan}^2}\left(\frac{r_1^2 + z_R^2}{f_{tan}^2} + \frac{2r_1}{\mu f_{tan}}\right)\right] \tag{45}$$

where $\Delta f_H = f_{L_H} - (r_{m2} - \mu f_{tan})$ and is small compared to the parameters it relates. By inspection of the image point position in (30), Δf_H is essentially the deviation from a point-to-parallel imaging of the slit into U11, for which $\Delta f_H = 0$. In the current design with $\Delta f_H > 0$ the monochromatic seed comes to a waist downstream of the SXRSS system, and then diverges downstream, as shown in Fig. 4. Thus the on-axis seed bandwidth also changes as the dispersed light propagates downstream. This is shown in Fig. 7, where the on-axis bandwidth evolves dynamically through the SXRSS transport before asymptotically settling approximately to the value given in Eq. (45). The chirp also varies in a related way, which is also shown.

The resolving power of the SXRSS system, given by the FWHM of the spectrum, is therefore

$$R = \frac{1}{2.35\sigma_{k,x=0}/k_0} \approx \frac{\pi N_0 w_0}{1.18 \sin\theta_i} \tag{46}$$

For $\Delta f_H = 0$ taken on the right, this is close to the value given in Ref. [23].

V. FRESNEL PROPAGATION

With Fresnel propagation integrals, one can model the evolution of an arbitrary paraxial field input through optical components that include higher order aberrations. Propagation through the system is calculated by applying the proper phase or amplitude transformation at each optical element and using Fresnel propagation integrals through the drifts and apertures. The procedure for the SXRSS system is outlined in Ref. [3], so we only quickly summarize it here.

To propagate over a drift of length z, the field at each frequency k is calculated according to the integral

$$E(\mathbf{r}_\perp, z) = \frac{ik}{2\pi z} e^{-ikz} \int E(\mathbf{r}'_\perp, 0) \exp\left[-i\frac{k}{2z}\left|\mathbf{r}_\perp - \mathbf{r}'_\perp\right|^2\right] d^2\mathbf{r}'_\perp. \tag{47}$$

where $\mathbf{r}_\perp$ is the transverse coordinate vector orthogonal to the direction of propagation. The effect of an optical element is modeled as a phase deformation,

$$E'(\mathbf{r}_\perp, z) = E(\mathbf{r}_\perp, z) \exp\left[i\Delta\Phi(\mathbf{r}_\perp)\right]. \tag{48}$$

The SXRSS system is modeled as a sequence of such transforms. Note that by the convolution theorem, this can also be done (often with greater numerical efficiency) with Fourier transforms in the spatial frequency domain of $\mathbf{r}_\perp$.

The phase shift $\Delta\Phi$ for the optical elements can be determined from the light path function and from the phases embedded in the Fresnel integrals. By comparing these and with the aid of the M matrix elements in (42), one can deduce that the phase deformation is

$$\Delta\Phi(x, y) = \frac{2\pi N_0}{\sin\theta_d}\frac{\Delta k}{k_0}x + \frac{k}{2\mu f_{tan}}x^2 + \frac{k}{2f_{sag}}y^2 - kC_{1,2}\frac{x}{\sin\theta_d}y^2 - kC_{3,0}\frac{x^3}{\sin^3\theta_d} \tag{49}$$

Note that the horizontal plane coordinate is rotated into the coordinate system of the outgoing diffracted ray. The effect of the grating is included by applying this phase to the field rescaled in the horizontal plane by $\mu = \sin\theta_d/\sin\theta_i$ at point P. Propagating a distance r_2 to the slit, the field at point B is then

$$E(\mathbf{r}_\perp, r_2) = \frac{ik}{2\pi r_2} e^{-ikr_2} \int E(x'/\mu, y', r_1) \exp\left[i\Delta\Phi(x', y') - i\frac{k}{2r_2}\left[(x - x')^2 + (y - y')^2\right]\right] dx'dy'. \tag{50}$$

This is straightforward to extend through the $M2$ mirror downstream.

VI. TWO-COLOR GRATING EQUATIONS

We now consider a grating that has an alternating pattern of groove densities in the x_0 direction to produce two colors. This patterning design was chosen as a simple practical way for the incident beam to encounter two different line densities in order that two colors within the FEL bandwidth colors go into the same diffraction angle. In this case we can describe the groove density in Eq. (8) as

$$N(x_0) = N_0 + \frac{\delta N}{2}\mathrm{sgn}\left(\sin\frac{2\pi x_0}{D}\right) + N_1 x_0 + N_2 x_0^2 \tag{51}$$

This square-wave pattern switches between densities $N_0^{(1)}$ and $N_0^{(2)}$ with difference $\delta N = N_0^{(2)} - N_0^{(1)}$ and period $D = 2\pi/\kappa$. For $2j\pi < \kappa x_0 < (2j+1)\pi$ the grating density is $N_0 + \frac{\delta N}{2} = N_0^{(2)}$, while for $(2j-1)\pi < \kappa x_0 < 2j\pi$ the grating density is $N_0 - \frac{\delta N}{2} = N_0^{(1)}$. The VLS aspect of the grating is maintained. The line density across the grating surface for the two color design with a $D = 250$ μm period and $\delta N = 10^{-3}N_0$=1.123 lines/mm density difference is shown in Fig. 8.

Using the condition $\frac{\partial F}{\partial x_0} = 0$ from Eq. (2) and the relation $\frac{dn}{dx_0} = N(x_0)$ from (8), the two-color grating equation is

$$\cos\theta_i - \cos\theta_d = m\lambda\left(N_0 \pm \frac{\delta N}{2}\right). \tag{52}$$

The relative difference in the line densities equals the relative color separation $\delta\omega = \omega_2 - \omega_1$,

$$\frac{\delta N}{N_0} = \frac{\delta\omega}{\omega_0}. \tag{53}$$

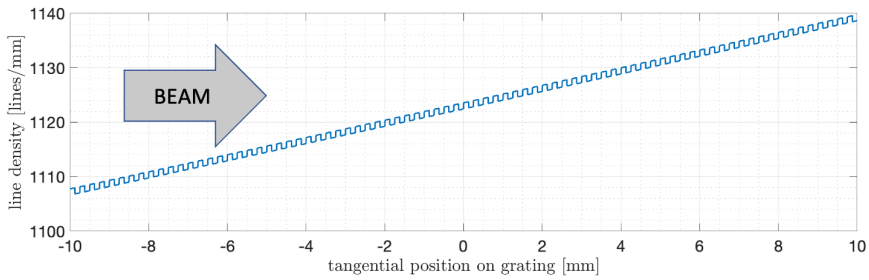

FIG. 8: Two color grating density across grating surface assuming a $D = 250$ μm period, $\delta N/N_0 = 0.1\%$, $N_1 = -1.6$ mm^{-2}, and $N_2 = 0.002$ mm^{-3}.

where $\omega_0 = (\omega_2 + \omega_1)/2$ is the average frequency. The two color x-ray seed spectrum and temporal profiles are shown in Fig. (9) where the color separation is set to be $\delta N/N_0 = 0.1\%$. This setting is chosen so that the two colors lie within the incoming SASE bandwidth such that reasonable power can be taken from each color to re-seed the FEL. To model the effect of re-seeding and overlap with the electron beam, the spectra and temporal profiles are calculated by integrating the seed fields along z in the downstream 3.3 m undulator over the round Gaussian electron beam transverse profile. Each color has the same relative bandwidth as the single color grating, even though each color hits half then number of grooves on the grating surface. This is because, in the unclosed optical dispersion design of the SXRSS system, the seed bandwidth is ultimately determined by the transport and overlap with the electron beam. The two colors interfere in the time domain to produce an intensity modulation with period $2\pi/\delta\omega = 2\pi N_0/\omega_0 \delta N$, which ranges from about 14 fs at 300 eV to 3.5 fs at 1200 eV for $\delta N/N_0 = 0.1\%$. It is interesting to note that, because of the quadratic phase structure and frequency chirp on the seed (see discussion in Sec. IV), the seed pulse duration is much larger than that expected from the inverse seed bandwidth. In the two color case, this leads to a pulse with more temporal modulations.

Figure 10 shows the dispersed profiles at the slit, assuming a $\sigma_\omega/\omega_0 = 10^{-3}$ bandwidth Gaussian input pulse at the grating for illustration. The two colors used for seeding are the portions that intersect the center $x = 0$ line, i.e., a narrow slit. Smaller sidebands are also produced at $\omega_{1,2} \pm \omega_0/DN_0$ due to the square-wave density variation. These sidebands can lie within the seeded FEL bandwidth to produce additional colors if $1/DN_0 < 2\rho$. To preserve the two color mode, this compels making D small enough to push the sidebands outside the FEL bandwidth. However, this must be balanced with minimizing the relative impact of the transition region between stripes if D is made too small. Assuming a transition region of about 10 μm, this gives a range of about $D = 100 - 400$ μm with a target of $D = 250$ μm for the SXRSS parameters.

Figure 11 shows the evolution of the spot size for the two color grating, for comparison with the one color case in Fig. 4. The two color design produces a much larger beam size in the horizontal plane, as expected.

Snapshots of the pulse intensity in the dispersive $x - \omega$ plane as the pulse propagates from the slit to inside the downstream undulator are shown in Figs. 12 and 13 for the 300 eV and 1200 eV cases, respectively. In the 300 eV case there is good color separation for a 40 μm wide slit. For 1200 eV, however, there is some frequency overlap, which is manifest as interference fringes at the spatial focus just downstream of M2. In both cases, the $\sigma_x = 28$ μm electron beam sees well-separated colors whose individual bandwidths shrink steadily along z as the dispersion dominated beam expands through the undulator. The resulting seed spectra and time profiles that overlap the e-beam are shown in Fig. 9.

Figure 14 shows the results of a seeded two-color XFEL simulation with GINGER on an ideal 65 fs tophat beam profile. We consider an LCLS-II beam with 1.5 kA, 0.4 MeV RMS energy spread and 0.4 μm emittance. The seed power in each color is 50 kW. In the initial stages of amplification, the FEL behaves as a linear amplifier so the FEL pulse mimicks the seed pulse shape; see Fig. 14 (top). As the FEL process starts to saturate (Fig. 14, middle), nonlinear growth reduces the fringe contrast, while radiation slippage effects shorten the temporal spike duration. Finally, in the post-saturation regime (Fig. 14, top), the pronounced spikes become about 1 fs FWHM in duration. Depending on the required application, we note that the number of temporal spikes can be adjusted in principle by manipulating the electron beam length, as afforded by the seed pulse duration. In addition, increasing the photon energy will result in larger absolute two-color separation, and per $2\pi N_0/\omega_0 \delta N$, will reduce the temporal spike durations.

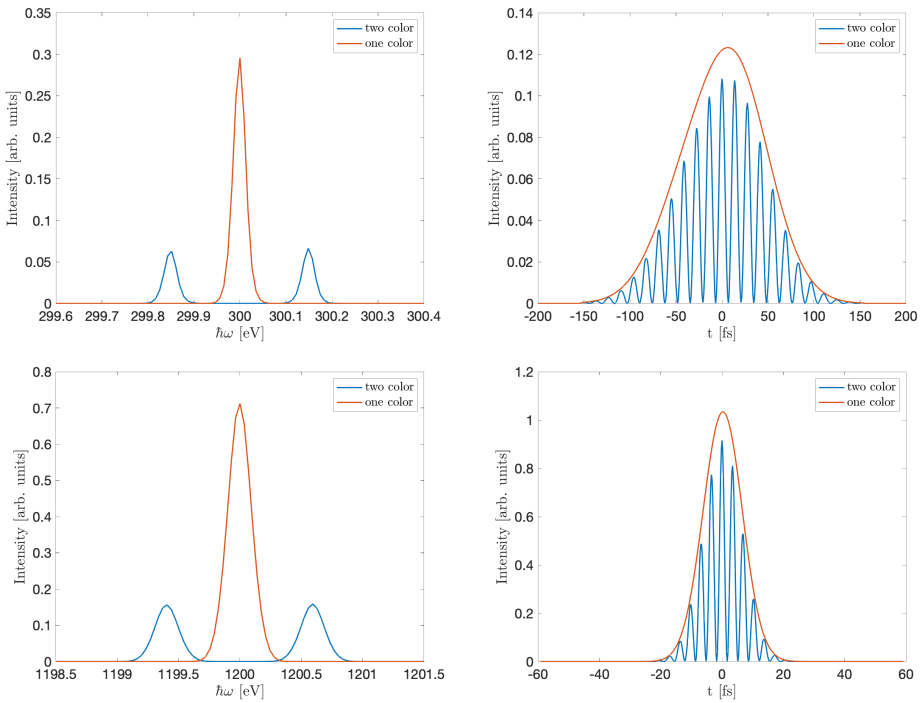

FIG. 9: Seed spectrum (left) and temporal pulse profile (right) from full transport simulations of the SXRSS system with torodial VLS single color (red) and two color (blue) gratings, integrated over the electron beam. Top: 300 eV central energy. Bottom: 1200 eV central energy.

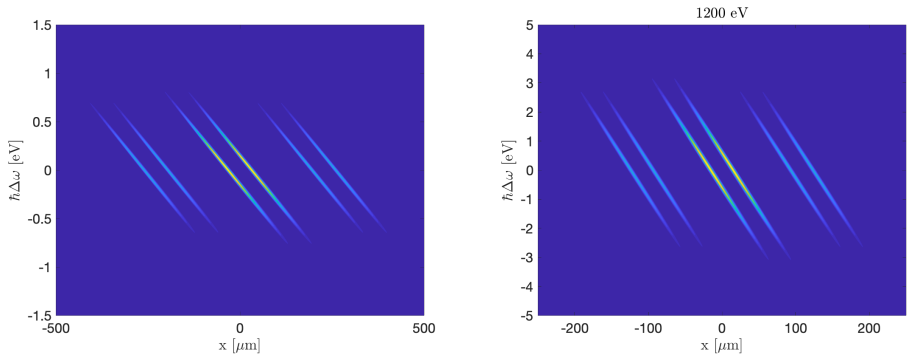

FIG. 10: Two color $x-\omega$ space at slit from $\sigma_\omega/\omega_0 = 10^{-3}$ bandwidth pulse at 300 eV (left) and 1200 eV (right). The alternating grating line density has $\delta N/N_0 = 0.01\%$ color separation and $D = 250$ μm period.

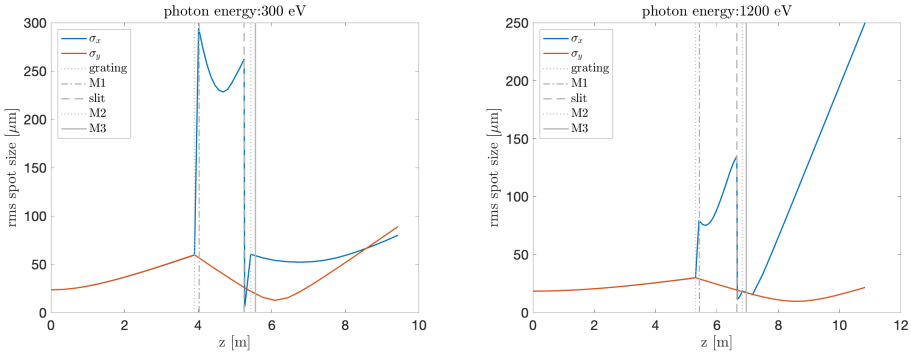

FIG. 11: Transverse x-ray beam envelope with two color grating at 300 eV (left) and 1200 eV (right) with 10 μm slit width.

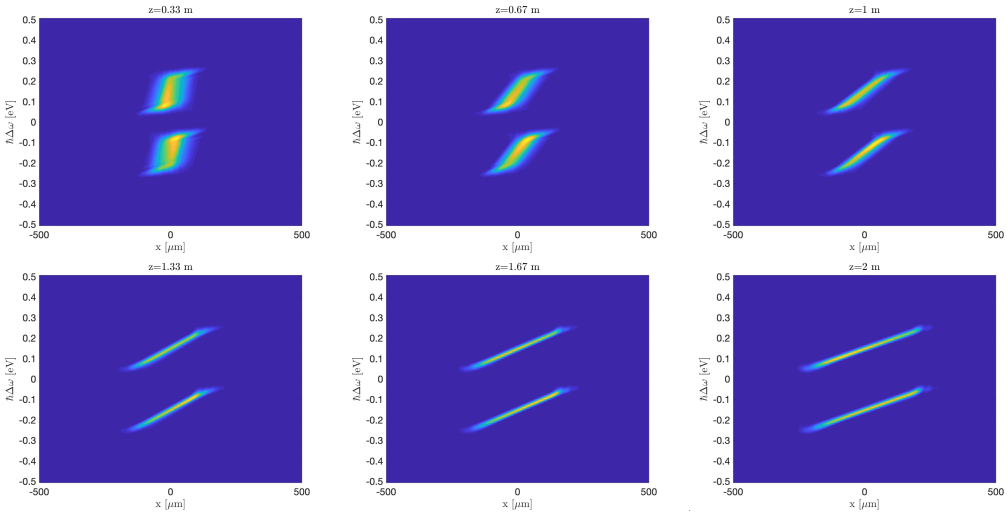

FIG. 12: Evolution of two color $x - \omega$ space at 300 eV from the $M2$ mirror to the entrance of the downstream undulator. A 40 μm wide slit is assumed.

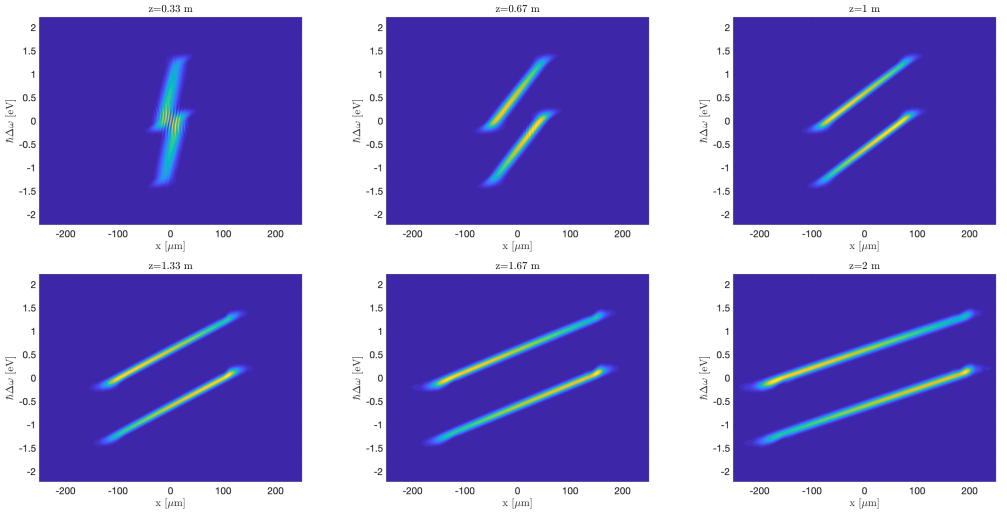

FIG. 13: Evolution of two color $x - \omega$ space at 1200 eV from the $M2$ mirror to the entrance of the downstream undulator. A 40 μm wide slit is assumed, for which the central frequencies from the two diffraction angles initially overlap.

VII. SUMMARY

We have presented the basic theory for the diffraction grating at the SXRSS at LCLS and LCLS-II. From the light path function, one is able to derive the basic grating diffraction and focusing properties. The ABCD matrix formalism is then examined, both for a monochromatic beam and for a finite pulse duration, which yields useful scaling and relations on the evolution of the transverse beam envelope, the image and waist locations, and the seed resolving power. We then introduce a design for two-color grating that contains an alternating pattern of grove densities to place two colors within the FEL bandwidth into the same forward diffraction angle, enabling two color FEL operations. We explored theoretically and numerically the grating properties, as well as the final seeded XFEL performance.

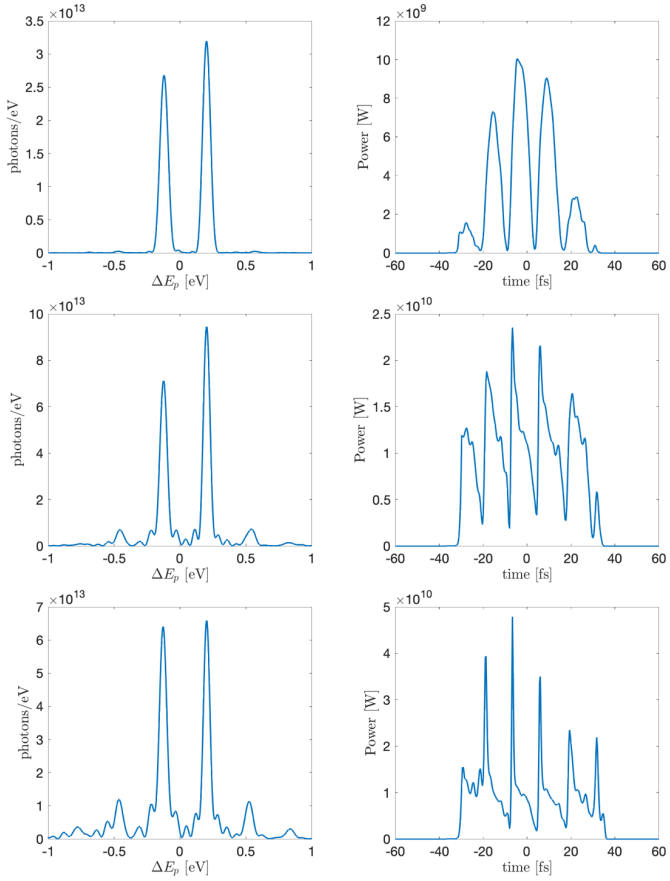

FIG. 14: GINGER simulation of two-color seeding at 310 eV (4 nm) with 0.31 eV separation in the exponential (top), saturation (middle) and post-saturation (bottom) regimes. Temporal pulse front is to the left.

VIII. ACKNOWLEDGEMENTS

We thank G. Wilcox, D. Cocco, D. Morton, D. Spiga, G. Marcus, and S. Serkez for helpful conversations. This work is supported by the U.S. Department of Energy Contract No. DE-AC02-76SF00515 and award no. 2017-SLAC-100382.

[1] D. Cocco, R. Abela, J. W. Amann, K. Chow, P. J. Emma, Y. Feng, G. L. Gassner, J. Hastings, P. Heimann, Z. Huang, et al., in *X-Ray Lasers and Coherent X-Ray Sources: Development and Applications X*, edited by A. Klisnick and C. S. Menoni, International Society for Optics and Photonics (SPIE, 2013), vol. 8849, pp. 31 – 38, URL https://doi.org/10.1117/12.2024402.

[2] Y. Feng, J. Amann, D. Cocco, C. Field, et al., in *Proceedings of FEL2012*, edited by T. Tanaka and V. Schaa (Nara, Japan, 2012).

[3] S. Serkez, J. Krzywinski, Y. Ding, and Z. Huang, Phys. Rev. ST Accel. Beams **18**, 030708 (2015), URL https://link.aps.org/doi/10.1103/PhysRevSTAB.18.030708.

[4] D. Ratner, R. Abela, J. Amann, C. Behrens, D. Bohler, G. Bouchard, C. Bostedt, M. Boyes, K. Chow, D. Cocco, et al., Phys. Rev. Lett. **114**, 054801 (2015), URL https://link.aps.org/doi/10.1103/PhysRevLett.114.054801.

[5] G. Marcus, W. M. Fawley, D. Bohler, Y. Ding, Y. Feng, E. Hemsing, Z. Huang, J. Krzywinski, A. Lutman, and D. Ratner, Phys. Rev. Accel. Beams **22**, 080702 (2019), URL https://link.aps.org/doi/10.1103/PhysRevAccelBeams.22.080702.

[6] E. Hemsing, A. Halavanau, and Z. Zhang, Phys. Rev. Accel. Beams **23**, 010701 (2020), URL https://link.aps.org/doi/10.1103/PhysRevAccelBeams.23.010701.

[7] Z. Zhang, G. Marcus, E. Hemsing, W. M. Fawley, Z. Huang, and A. Lutman, Phys. Rev. Accel. Beams **23**, 010704 (2020), URL https://link.aps.org/doi/10.1103/PhysRevAccelBeams.23.010704.

[8] E. Hemsing, G. Marcus, W. M. Fawley, R. W. Schoenlein, R. Coffee, G. Dakovski, J. Hastings, Z. Huang, D. Ratner, T. Raubenheimer, et al., Phys. Rev. Accel. Beams **22**, 110701 (2019), URL https://link.aps.org/doi/10.1103/

PhysRevAccelBeams.22.110701.
[9] A. G. Kostenbauder, IEEE Journal of Quantum Electronics **26**, 1148 (1990).
[10] B. Hajj, L. Oudjedi, J.-B. Fiche, M. Dahan, and M. Nollmann, Scientific Reports **7**, 5284 (2017), ISSN 2045-2322, URL https://doi.org/10.1038/s41598-017-05531-6.
[11] D. C. Skigin and R. A. Depine, Appl. Opt. **46**, 1385 (2007), URL http://ao.osa.org/abstract.cfm?URI=ao-46-9-1385.
[12] A. Lutman, F.-J. Decker, J. Arthur, M. Chollet, Y. Feng, J. Hastings, Z. Huang, H. Lemke, H.-D. Nuhn, A. Marinelli, et al., Physical review letters **113**, 254801 (2014).
[13] E. Hemsing, A. Halavanau, and Z. Zhang, Phys. Rev. Lett. **125**, 044801 (2020), URL https://link.aps.org/doi/10.1103/PhysRevLett.125.044801.
[14] N. Sudar, R. Coffee, and E. Hemsing, Phys. Rev. Accel. Beams **23**, 120701 (2020), URL https://link.aps.org/doi/10.1103/PhysRevAccelBeams.23.120701.
[15] G. Geloni, V. Kocharyan, T. Mazza, M. Meyer, E. Saldin, and S. Serkez, *Opportunities for two-color experiments at the sase3 undulator line of the european xfel* (2017), 1706.00423.
[16] N. Berrah, A. Sanchez-Gonzalez, Z. Jurek, R. Obaid, H. Xiong, R. J. Squibb, T. Osipov, A. Lutman, L. Fang, T. Barillot, et al., Nature Physics **15**, 1279 (2019), ISSN 1745-2481, URL https://doi.org/10.1038/s41567-019-0665-7.
[17] S. Schreck, E. Diesen, J. LaRue, H. Ogasawara, K. Marks, D. Nordlund, M. Weston, M. Beye, F. Cavalca, F. Perakis, et al., The Journal of Chemical Physics **149**, 234707 (2018), https://doi.org/10.1063/1.5044579, URL https://doi.org/10.1063/1.5044579.
[18] T. Harada, H. Sakuma, K. Takahashi, T. Watanabe, H. Hara, and T. Kita, Appl. Opt. **37**, 6803 (1998), URL http://ao.osa.org/abstract.cfm?URI=ao-37-28-6803.
[19] A. E. Siegman, Journal of the Optical Society of America A **2**, 1793 (1985).
[20] M. A. Porras, J. Alda, and E. Bernabeu, Appl. Opt. **31**, 6389 (1992), URL http://ao.osa.org/abstract.cfm?URI=ao-31-30-6389.
[21] E. Hemsing, Ph.D. thesis, University of California Los Angeles (2011).
[22] G. Marcus, Opt. Express **24**, 7752 (2016), URL http://www.opticsexpress.org/abstract.cfm?URI=oe-24-7-7752.
[23] S. Serkez, p. 143 (2015), URL http://xfel.tind.io/record/139.